INORGANIC CHEMISTRY FRONTIERS

RESEARCH ARTICLE

View Article Online
View Journal | View Issue

Cite this: *Inorg. Chem. Front.*, 2024, **11**, 8753

Simple aliovalent cation substitution to induce strong optical anisotropy enhancement in a rare thioantimonate(v) family†

Qixian Ren,[a,b] Wangfei Che,[b] Mengmeng Chen,[b] Chen Cui,*[b] Yabo Wu *[b] and Zhi Su*[a]

Thioantimonates containing high oxidation state Sb^{5+} have been proven to exhibit excellent performance in the design of new materials such as infrared optical crystals and lithium-ion batteries. However, as described by the "inert pair effect", the preparation of P-block elements containing high oxidation states in sealed systems has been a challenge. In this study, an aliovalent cation substitution strategy was used to design and synthesize three novel thioantimonates(v), $A_4BaSb_2Se_8$ (A = Cs, Rb) and Rb_2BaSbS_4Cl (RBSSC), respectively, all of which contain rare $[SbS_4]$ tetrahedral units. The introduction of Ba^{2+} ions leads to the distortion and high-density arrangement of $[SbSe_4]$ units, which is manifested as a significant 3.7 times enhancement of the birefringence compared to that of the parent compound Cs_3SbSe_4 (0.041 → $Cs_4BaSb_2Se_8$ 0.150@1064 nm). By further introducing highly electronegative halogen atoms, the first antimony-based thiohalide(v) RBSSC was synthesized. Theoretical calculations show that the band gap of RBSSC is up to 3.674 eV, larger than those of all known antimony-based thiohalides(iii). This work provides strong evidence that the aliovalent cation substitution strategy is an effective way to find new thioantimonate(v) families, and also indicates that the cation size effect introduced by elemental substitution may lead to surprising performance improvements.

Received 9th September 2024,
Accepted 8th November 2024

DOI: 10.1039/d4qi02280g

rsc.li/frontiers-inorganic

Introduction

Recently, antimony (Sb)-based chalcogenides have become one of the hotspots for designing optical materials due to their rich coordination environments and wide transparency range in the infrared region.[1–5] Many high-performance thioantimonates have been reported to date, including Cu_3SbS_4, $K_2Sb_4S_7$, Cu_2ZnSbS_4, $Ba_4GeSb_2Se_{11}$ and $Ba_3La_4Ga_2Sb2S_{15}$.[6–10] With an incident laser wavelength of 2.05 μm, $Ba_{23}Ga_8Sb_2S_{38}$ exhibits the highest intensity of powder second harmonic generation (SHG) among the reported sulfide infrared nonlinear optical materials, which is about 22 times stronger than that of commercially available $AgGaS_2$.[11] Furthermore, the introduction of the Sb^{3+} cation with stereochemically active lone pair electrons has been proven to be an effective strategy to enhance the birefringence of materials. $LiSrSbS_3$ with a parallel configuration of $[SbS_3]$ units exhibits a giant birefringence of 0.238@1064 nm.[12] However, these studies have mainly focused on thioantimonates(iii), while the synthesis and structure–property relationships of thioantimonates(v) have rarely been reported.[13]

Changes in the valence states lead to different electronic configurations, which alter the coordination and charge densities within the framework.[14,15] The oxidation states of Sb are typically observed in the form of Sb^{3+} or Sb^{5+} cations. The valence electron configuration of Sb^{3+} is $(n-1)d^{10}\ 5s^2$, and it typically adopts trigonal pyramidal, seesaw, and octahedral configurations. Conversely, the valence electron configuration of Sb^{5+} is $(n-1)d^{10}$, resulting in all configurations being regular tetrahedral structures. Building blocks with different coordination modes exhibit distinct cohesive behaviours, which will affect the macroscopic properties of materials. Previous studies on Sb-based infrared optical materials have tended to surround Sb^{3+} with stereochemically active lone-pair electrons, which can be considered a major contributor of the nonlinear optical effect and optical anisotropy. However, in addition to its high toxicity, Sb^{3+} is incapable of forming a tetrahedral functional unit, which can be considered an

[a]*College of Chemistry and Chemical Engineering, Xinjiang Normal University, Urumqi, 830054 Xinjiang, PR China. E-mail: suzhixj@163.com*
[b]*Research Center for Crystal Materials; State Key Laboratory of Functional Materials and Devices for Special Environmental Conditions; Xinjiang Key Laboratory of Functional Crystal Materials; Xinjiang Technical Institute of Physics and Chemistry, Chinese Academy of Sciences, 40-1 South Beijing Road, Urumqi 830011, China. E-mail: wyb@ms.xjb.ac.cn, cuichen@ms.xjb.ac.cn*

†Electronic supplementary information (ESI) available. CCDC 2380614–2380616. For ESI and crystallographic data in CIF or other electronic format see DOI: https://doi.org/10.1039/d4qi02280g

advanced fundamental building block for infrared optical materials.[16] Theoretical calculations suggest that the [SbQ_4] (Q = S/Se) tetrahedron has a larger HOMO–LUMO band gap compared to [SbQ_3], rocking-chair-like [SbQ_4] units, and [SbQ_5] units (Fig. S1†). Moreover, thioantimonates with high oxidation state Sb^{5+} also show potential in the field of such superconducting sulfides and lithium-ion battery preparation.[17–19] Therefore, it is necessary to study the synthesis and physicochemical properties of Sb^{5+}.

As shown in Fig. 1, we surveyed all fully occupied Sb-based chalcogenides in the Inorganic Crystal Structure Database (ICSD). The synthesis of these compounds typically occurs within a sealed system. Around 90.8% of the compounds exhibit Sb with a valence state of +3, while only 17 cases demonstrate a valence state of +5. These compounds belong to $M_{3-x}M'_xSbQ_4$ and $M_3Ag_2Sb_3Q_8$ (M = K, Na, Rb, Cs, Au, Ag, Cu; Q = S, Se) families (Table S15†).[20–23] As described by the "inert pair effect" observed in P-block heavy elements, the formation of Sb^{5+} is difficult in chalcogenides and halides.[24] This can be attributed to the insufficient shielding of the atomic nucleus in Sb, leading to the contraction of d orbitals and lowering of the 5s orbital energy level.[25] As a result, promoting an electron from the $5s^2$ orbital to form Sb^{5+} becomes more difficult, leading to the fact that obtaining Sb-based chalcogenides with a high oxidation state (Sb^{5+}) in vacuum-sealed systems has been a challenge.

In this work, a new family of thioantimonate(v) compounds with [SbQ_4] tetrahedra was successfully synthesized in a sealed system by employing an aliovalent cation substitution strategy. We systematically investigated the material synthesis and physical properties of CBSS and RBSS, as well as the structural evolution of the parent compound Cs_3SbSe_4 (CSS). The compound CBSS showed a significant enhancement of optical anisotropy (birefringence 0.041 → 0.150@1064 nm) compared to the parent compound CSS. The remarkable optical anisotropy exhibited by the CBSS compound suggests that it holds promise for applications in mid-infrared optical devices, such as lidar, environmental monitoring and functional group detection instruments.[26,27] Furthermore, through the introduction of halogens with higher electronegativity, we achieved the first synthesis of antimony-based thiohalides(v), Rb_2BaSbS_4Cl (RBSSC). This study provides a valuable reference for the synthesis of thioantimonate(v) and elucidates its structure–performance relationship.

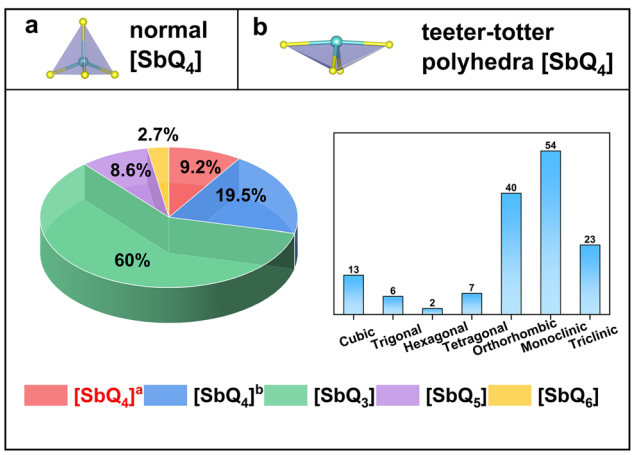

Fig. 1 Coordination patterns and crystal system distribution of thioantimonate.

Experimental section

Reagents

All the raw materials (RbCl, CsCl, Ba, Sb, Se, and S) were purchased from Shanghai Aladdin Biochemical Technology Co., Ltd with purities higher than 99.99% and kept in a dry air-filled glove-box with restricted oxygen and moisture levels below 0.1 ppm. The entire weighing process was carried out in the glove-box to avoid the reaction between the metals and oxygen in the air.

Synthesis of title compounds

All the raw materials were used as purchased without further refinement. In the preparation process, a graphite crucible was added into the vacuum-sealed silica tube evacuated to 10^{-3} Pa to avoid the reaction between halides (ACl) and silica tube at high temperatures. $A_4BaSb_2Se_8$ (A = Rb, Cs) was prepared with a mixture under an Ar atmosphere in a glovebox at the stoichiometric ratio of ACl : Ba : Sb : Se = 3 : 2 : 1 : 6, respectively. The temperature process was set as follows: first, a microchip-controlled furnace was heated to 400 °C for 12 h, to avoid latent explosion of the silica tube derived from the high vapor pressure of element S at 440 °C. One critical step was chosen: held at 400 °C for 7 h to achieve the reaction of partial S/Se. Subsequently, the furnace was heated to 850 °C over a period of 20 hours and then annealed at 850 °C for 2 days. After the annealing step, the sample was cooled to 400 °C at a rate of 3 °C per hour and cooled down to room temperature over the course of 24 hours. This process resulted in the successful synthesis of a brown single crystal of the titled compound $A_4BaSb_2Se_8$.

Rb_2BaSbS_4Cl: The raw materials RbCl, Ba, Sb, and S were weighed and loaded into graphite crucibles in a ratio of 3 : 3 : 1 : 7. The preparation process was like that of $A_4BaSb_2Se_8$. The maximum reaction temperature was set at 900 °C. Finally, numerous yellow crystals of Rb_2BaSbS_4Cl were also obtained and remained stable in the air.

Single-crystal structure determinations

High-optical quality crystals ($Rb_4BaSb_2Se_8$, 0.131 × 0.078 × 0.07 mm^3 and $Cs_4BaSb_2Se_8$, 0.054 × 0.134 × 0.082 mm^3 and Rb_2BaSbS_4Cl 0.039 × 0.133 × 0.154 mm^3) were selected under an optical microscope and used for single-crystal X-ray data collection (Fig. S2†). At room temperature, crystal data collection was conducted using a Bruker SMART APEX III CCD single crystal X-ray diffractometer with graphite-monochroma-

tized molybdenum Mo Kα radiation (λ = 0.71073 Å). After collection, the SADABS program was used to perform the multi-scan type absorption correction of the structural data.[28,29] After that, the XPREP program in the SHELXTL program package was used to determine the space group, while the SHELXT and XL programs were applied to solve and refine the structural data by direct methods and full-matrix least-squares on F^2. The structures were checked with PLATON,[30] revealing the absence of any additional higher symmetry elements.

Powder X-ray diffraction

The powder X-ray diffraction (PXRD) measurements were performed using a Bruker D2 PHASER diffractometer with Cu Kα radiation (λ = 1.5418 Å) at room temperature. The PXRD data were collected with a 2θ range from 10 to 70° and a scan step rate of 0.02°. The theoretical XRD patterns were obtained using Mercury software based on their CIF files.

UV-Vis-NIR diffuse-reflectance spectroscopy

The optical diffuse-reflectance spectra of the RBSS were recorded at room temperature using a Shimadzu SolidSpec-3700DUV spectrophotometer. The measured wavelength range was 200–2600 nm. To figure out the experimental band gap (E_g), the diffuse reflection data are converted into absorption data using the Kubelka–Munk function $F(R) = K/S = (1 - R)^2/2R$,[31] where R represents the reflection coefficient, K is the absorption value, and S is the scattering coefficient.

Raman spectroscopy

The selected RBSS crystal was first placed on a glass slide, followed by irradiation with a 532 nm laser on the sample. The Raman spectra in the range of 40–4000 cm^{-1} were recorded using the LABRAM HR Evolution spectrometer equipped with a CCD detector. The integration time was configured to 5 seconds, and the laser intensity was maintained at 5%.

Energy-dispersive X-ray spectroscopy analyses

To determine the chemical compositions, the EDS spectra and mappings of three compounds were tested on a field emission scanning electron microscope (FE-SEM, JEOL JSM-7610F Plus, Japan) equipped with an energy-dispersive X-ray spectrometer (Oxford, X-Max 50).

Computational description

The pseudo-potential plane wave approach in the density functional theory (DFT) was used to explain the electron structure and its correlation between optical characteristics and the crystal structure by the first-principles calculations.[32,33] The exchange and correlation effects were evaluated using the generalized gradient approximation (GGA) method,[34] with the Perdew–Burke–Ernezehof (PBE) function.[35] The electronic structure and optical properties were calculated by using the norm-conserving pseudopotential (NCP). The Cs-$6s^1$, Rb-$5s^1$, Ba-$6s^2$, Sb-$5s^25p^3$, Se-$4s^24p^4$, S-$3s^23p^4$ and Cl-$3s^23p^5$ were treated as the valence electrons.[36] Kinetic energy cut-offs were set to be 440.0 eV and Monkhorst–Pack k-point meshes (2 × 3 × 3) with a density of fewer than 0.3 $Å^{-1}$ in the Brillouin zone (BZ) were adopted. The computational parameters and convergence criteria in the CASTEP code were set to their default values, which have been demonstrated to be sufficiently accurate for our current calculations. In order to obtain a more precise HSE 06 band gap, we employed the Heyd–Scuseria–Ernzerhof (HSE 06) hybrid functional with a plane wave cutoff of 50 Ryd.[37,38]

To calculate the birefringence, the complex dielectric function $\varepsilon(\omega) = \varepsilon_1(\omega) + i\varepsilon_2(\omega)$ was computed from the PBE wave functions. The imaginary portion of the dielectric function ε_2 may be estimated upon the electronic structures, and its real part is determined using the Kramers–Kronig transform, which was used to derive the refractive indices and finally get the birefringence Δn; the band gap difference calculated using the HSE06 and GGA methods is utilized as the scissor operator to calculate the birefringence. The scissor operator values for RBSS and RBSSC are 0.41 and 0.84 eV, respectively.

Results and discussion

Crystal structures

The compound $A_4BaSb_2Se_8$ (A = Cs, Rb) was synthesized *via* high-temperature solid-state reaction in a sealed quartz tube, and the detailed chemical synthesis procedure can be found in the experimental section. Crystal data and refinement parameters, atomic coordinates and equivalent isotropic displacement parameters, as well as bond lengths and angle information are provided in Tables S1–S14.† The results of single-crystal X-ray diffraction indicate that $A_4BaSb_2Se_8$ (A = Cs, Rb) possess an isostructural relationship; thus, only the crystal structure of $Cs_4BaSb_2Se_8$ (CBSS) is elaborated in detail. CBSS adopts an orthorhombic space group *Ibam* (No. 72), with lattice parameters a = 20.2919(12) Å, b = 9.9957(6) Å, c = 11.0708(6) Å, and Z = 4. In the asymmetric unit, there are two Cs atoms, one Ba atom, one Sb atom, and three Se atoms. Each Cs atom and Ba atom are coordinated with eight Se atoms to form [$CsSe_8$] and [$BaSe_8$] polyhedra with bond lengths of d_{Cs-Se} = 3.480–4.227 Å and d_{Ba-Se} = 3.441–3.481 Å (Fig. 2a–c). The Sb atom forms a typical [$SbSe_4$] tetrahedron by bonding with four Se atoms (Fig. 2e), with a bond length of d_{Sb-Se} = 2.453–2.477 Å. The calculated bond valence sums (BVS) (Cs: 0.72–1.16, Ba: 1.66, Sb: 5.39, Se: 2.13–2.17) confirm the rationality of the crystal structure (Table S2†). The CBSS exhibits unique structural features characterized by the arrangement of Cs^+ and Ba^{2+} cations in a three-dimensional framework, forming one-dimensional $[Cs1Se_4]_\infty$ chains and $[BaSe_5]_\infty$ chains, which are separated by inserted two-dimensional $[Cs2Se_4]_\infty$ layers referred to as chain I, chain II, and layer I. Furthermore, the incorporation of isolated [SbS_4] tetrahedra results in the formation of a well-organized three-dimensional framework (Fig. 2d).

The single crystal of Rb_2BaSbS_4Cl was synthesized using the same method. RBSSC crystallizes in the monoclinic space group

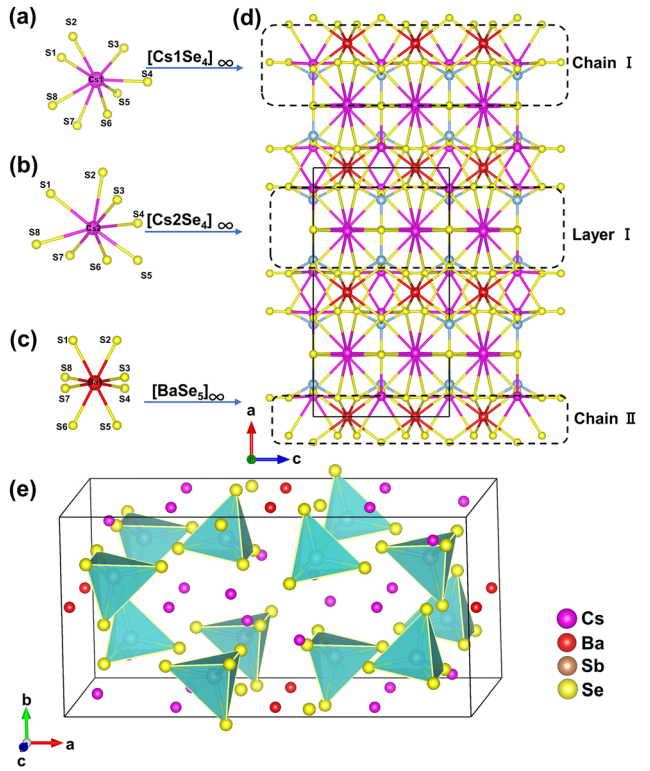

Fig. 2 (a and b) The connection mode of Cs in CBSS; (c) the connection mode of Ba in CBSS; (d) crystal structure of CBSS along the *b*-axis; and (e) the CBSS structure consisting of discrete [$SbSe_4$] tetrahedra.

$P2_1/c$ (No. 14). The cell parameters were determined as follows: a = 10.1114(15) Å, b = 9.0493(13) Å, c = 12.3826(16) Å, β = 90.382(6) Å, and Z = 4. The asymmetric unit contains two crystallographically independent Rb atoms, one Ba atom, one Sb atom, four S atoms, and one Cl atom. Rb1 atom is coordinated by six S atoms and two Cl atoms, while Rb2 atom is surrounded by seven S atoms and two Cl atoms. The bond lengths for d_{Rb-S} and d_{Rb-Cl} are 3.189–3.914 Å and 3.298–3.973 Å, respectively. The Sb atom forms [SbS_4] tetrahedra with four S atoms and the bond length is d_{Sb-S} = 2.291–2.333 Å; these values are typical for sulfides.[39,40] RBSSC is composed of two-dimensional layers (1) formed by sharing S atoms between the [RbS_6Cl_2] and [RbS_7Cl_2] units. The S and Cl atoms in two opposing $[BaS_5Cl_2]_\infty$ infinite chains are bridged and interconnected, resulting in the formation of a two-dimensional layer (2). Isolated [SbS_4] tetrahedra are embedded between layers to form a three-dimensional structure of Rb_2BaSbS_4Cl (Fig. S3†).

Through a strategy of aliovalent cation substitution, the structural transformation from CSS to CBSS was achieved. (Fig. 3a and b). From a perspective of structural chemistry, the quaternary CBSS can be regarded as a derivative of the ternary CSS through partial aliovalent substitution. This substitution occurs in the form of one Ba atom replacing two Cs atoms and forming one-dimensional chains connected by shared Se atoms that are inserted into the anionic framework, resulting in an elevation of the space group from *Pnma* to *Ibam* (Fig. 3c and d), effectively increasing the volume of the crystal unit cell and enhancing the density of birefringent functional units. The structural variation in CBSS can be attributed to chemical pruning driven by Ba^{2+} cations.

Optical properties

The experimental powder X-ray diffraction (PXRD) data in good agreement with theoretical results obtained from single crystal analysis, except for two weak peaks that may be attributed to impurities of $CsCl_2$ (PDF 24-0095) and Sb_2Se_3 (PDF 15-0861) (Fig. 4a). The polycrystalline CBSS powder sample was heated to 850 °C and kept for 30 h, then cooled down to room temperature in a muffle furnace. The XRD pattern after melting corresponds to the pattern observed before melting, demonstrating that CBSS is a congruent-melting compound. Quantitative analysis using energy-dispersive spectroscopy (EDS) reveals an atomic ratio of Cs : Ba : Sb : Se as 18.97 : 7.39 : 12.96 : 60.68, which approximates the stoichiometric ratio of CBSS with a chemical formula of 4 : 1 : 2 : 8 (Fig. S4†). The BVS calculation reveals that all Sb cations exhibit an oxidation state of +5. The oxidation state of Sb was determined through X-ray photoelectron spectroscopy (XPS), which shows a spin–orbit doublet consisting of Sb $3d_{3/2}$ and Sb $3d_{5/2}$, corresponding to two peaks observed at 530.3 eV and 539.7 eV in the Sb 3d region (Fig. 4b), respectively. These peak locations align with previously reported literature, confirming the presence of Sb^{5+}.[41] The diffuse reflectance spectrum of polycrystalline powder samples was measured across the ultraviolet-visible-near-infrared range in order to assess the band gap. Based on the Kubelka–Munk function analysis,[42–44] it was determined that RBSS possesses a band gap of 2.00 eV, with a UV cutoff edge below 582 nm (Fig. 4c). To further corroborate the presence of the [$SbSe_4$] unit, Raman scattering spectrum of CBSS was acquired using 532 nm excitation on a LABRAM HR Evolution spectrometer equipped with a CCD detector. As shown in Fig. 4d, the peaks observed at 215 cm^{-1} can be attributed to the stretching vibrations of Sb–Se chemical bonds.[45] The Raman spectra of both RBSS and RBSSC were simultaneously examined, thereby providing supplementary evidence to support our findings (Fig. S5†).

The electronic configurations, optimized structural models, and lattice parameters of $A_4BaSb_2Se_8$ (A = Cs, Rb) and Rb_2BaSbS_4Cl were determined through first-principles calculations, aiming to investigate the structure–property relationship. The CBSS, RBSS, and RBSSC compounds exhibit band gaps of 2.063, 1.918, and 2.829 eV, respectively (Fig. 5a–c). Among them, CBSS and RBSS are categorized as direct band gap semiconductors, while RBSSC is classified as an indirect band gap semiconductor. The electron localization function (ELF) is used to characterize the localized behavior of electrons and reveal subtle distinctions in their distribution.[46] The spherical appearance of electron localization around Cs atoms in CBSS and separated from [$SbSe_4$] clusters, indicates that the localized Cs atoms exhibit pronounced ionic properties. The continuous expansion of delocalization suggests that the formation of Sb–Se covalent bonds makes it easier for electrons to transfer, which is the reason for the increased band gap in

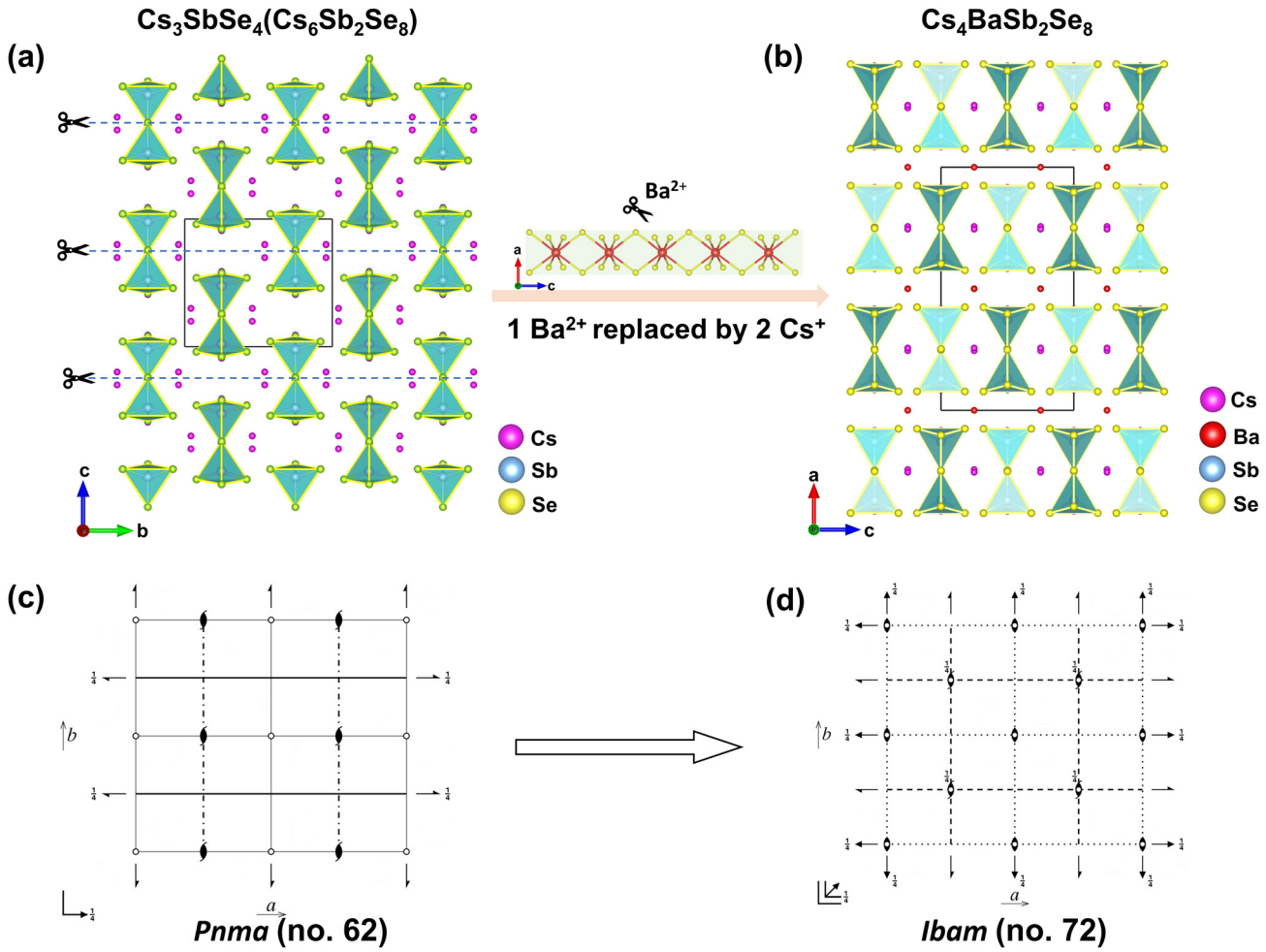

Fig. 3 (a and b) Structural evolution from (a) Cs_3SbSe_4 to (b) $Cs_4BaSb_2Se_8$ based on an aliovalent-cation-substitution-induced strategy; and (c and d) the spatial symmetry operation change from CSS [low symmetry *Pnma* (no. 62)] to CBSS [high symmetry *Ibam* (no. 72)].

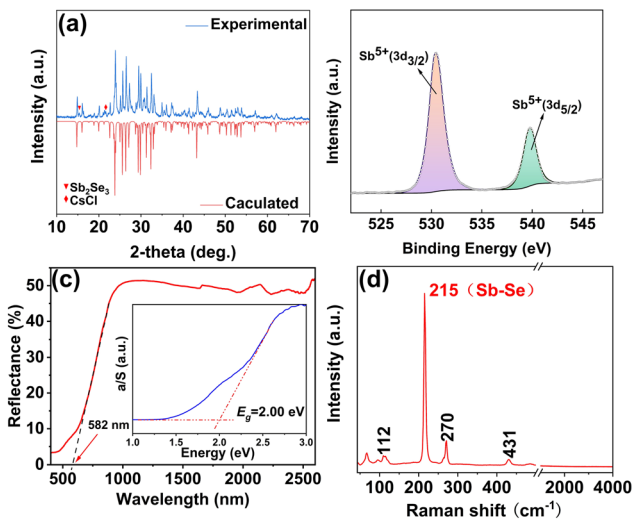

Fig. 4 (a) PXRD patterns of CBSS; (b) XPS spectrum of the CBSS sample; (c) UV-vis-NIR diffuse spectrum and experiment band gap; and (d) the Raman spectrum of CBSS.

CBSS (Fig. S6†). In order to investigate the influence of structural evolution on the performance, the optical properties of the parent compound CSS were also calculated. The GGA band gap of the CSS compounds is 1.933 eV, indicating a slight enhancement of the band gap of the compounds after aliovalent cation substitution (Fig. S7†).

Owing to the discontinuity of the exchange-related energy function, GGA band gaps are typically underestimated in calculations.[47–49] Consequently, we conducted a comprehensive investigation and computation of the HSE 06 band gaps for RBSS and RBSSC compounds. The calculated band gap of RBSS is 2.331 eV, while that of RBSSC is 3.674 eV, indicating that the introduction of the more electronegative halogen element has successfully increased the band gap.[50] The total and partial density of states (TDOS and PDOS) curve clearly illustrates the contributions of different orbitals from constituent elements to the electronic band structure.[51–53] In CBSS, the valence band maximum (VBM) is predominantly governed by Se-3p orbitals, while the conduction band minimum (CBM) is primarily influenced by both Se-3p and Sb-5p orbitals

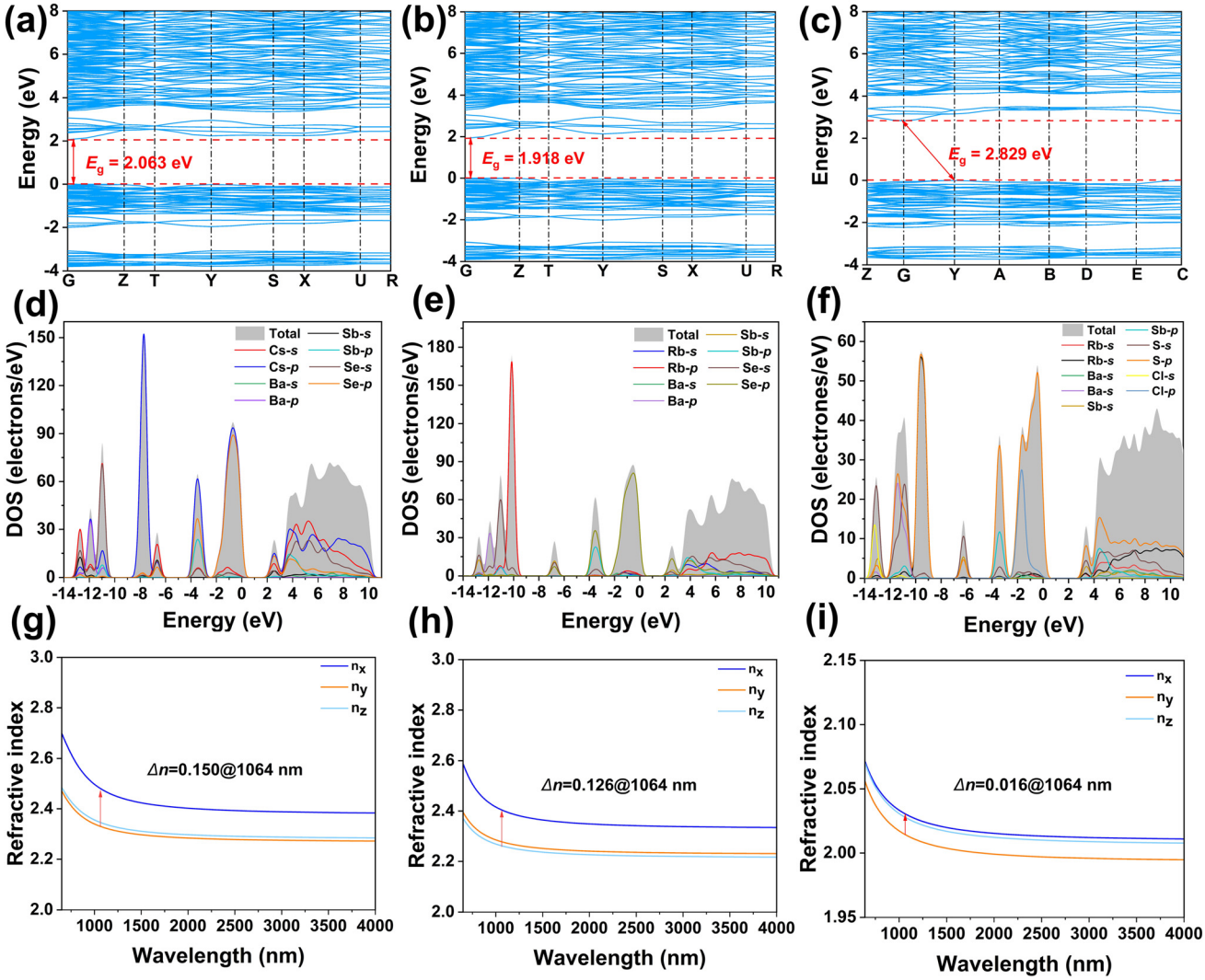

Fig. 5 (a–c) The calculated electronic band structure of CBSS, RBSS and RBSSC; (d–f) total and partial density of states with the energy region from −14 to 10 eV; and (g–i) calculated refractive index dispersion curves and birefringence of CBSS, RBSS and RBSSC.

(Fig. 5d and e). In RBSSC, the VBM is dominated by Se-3p and Cl-3p orbitals, whereas the CBM is mainly influenced solely by Se-3p (Fig. 5f). Consequently, charge transitions in CBSS and RBSSC are regulated by covalent bands formed between Sb–Se and Sb–S bonds, which significantly dictate their optical properties. Since the refractive index and birefringence of crystals are important parameters for the fabrication of mid-infrared laser devices, the refractive index dispersion curves of the title compounds in the range of 500–4000 nm were calculated.[54,55] It can be observed that at 1064 nm, CBSS exhibits a significant birefringence of 0.150, RBSS demonstrates a value of 0.126, while RBSSC shows a considerably lower value of 0.016.

In order to further elucidate the relationship between the structure and optical properties, we evaluated the density and distortion level of [$SbSe_4$] units in CSS and CBSS compounds. The results show that along with the introduction of Ba^{2+} ions, the density of [$SbSe_4$] in CSS and CBSS is raised from 2.33 × 10^{-3} to 3.56 × 10^{-3} Å^{-3}. Meanwhile, the distortion level of the [$SbSe_4$] tetrahedron is significantly improved (Fig. 6a). It successfully increases the birefringence of the host compound from 0.041@1064 nm (CSS) to 0.150@1064 nm (CBSS) due to the size effect from cation substitution (Fig. 6b). This work provides strong evidence that increasing functional unit

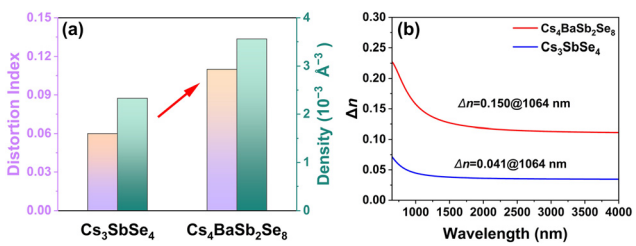

Fig. 6 (a) Comparison of the tetrahedral distortion index and functional unit density between CSS and CBSS; and (b) the calculated birefringence of CSS and CBSS.

density or adjusting distortion level in the crystal structure serves as an effective strategy for enhancing optical properties.[56]

Conclusion

In this work, three novel thioantimonate(v) compounds containing $[SbQ_4]$ tetrahedra of $Cs_4BaSb_2Se_8$ (CBSS), $Rb_4BaSb_2Se_8$ (RBSS), and Rb_2BaSbS_4Cl (RBSSC) were successfully synthesized in a sealed system through an aliovalent cation substitution strategy. By studying the single-crystal structures and optical properties of these three compounds, it is shown that the introduction of the $[BaSe_5]_\infty$ coordination polyhedron leads to a high-density arrangement of the $[SbSe_4]$ units, which significantly enhances the optical anisotropy compared to the parent compound Cs_3SbSe_4. Meanwhile, the HSE 06 band gap of RBSSC is up to 3.674 eV, which is larger than those of all known antimony-based thiohalides(III). Overall, this work not only expands the structural and chemical diversity of Sb-based chalcogenides but also provides valuable insights into the structure–property relationships governing the optical performance of these materials. The successful synthesis of Sb^{5+} containing chalcogenides paves the way for further exploration and development of novel infrared optical materials.

Author contributions

Zhi Su and Yabo Wu supervised the research and revision of the manuscript. Qixian Ren designed and performed the experiments and wrote the first draft and revised it. Wangfei Che performed the theoretical calculations. Chen Cui and Mengmeng Chen assisted with the experimental work. All authors participated in the discussion.

Data availability

The authors confirm that the data supporting the findings of this study are available within the article and its ESI.† CCDC 2380614–2380616† contain the supplementary crystallographic data for this paper.

Conflicts of interest

The authors declare no conflict of interest.

Acknowledgements

This work is supported by the Natural Science Foundation of the Xinjiang Uygur Autonomous Region (2022D01B206 and 2023D01A04), Shanghai Cooperation Organization Science and Technology Partnership Program (2023E01001), and the National Natural Science Foundation of China (62305382 and 52302011). Y. W. and C. C. are thankful for the support from Tianchi Doctor Plan of Xinjiang Uygur Autonomous Region.

References

1 B. B. Su, S. N. Geng, Z. W. Xiao and Z. G. Xia, Highly distorted antimony(III) chloride $[Sb_2Cl_8]^{2-}$ dimers for near-infrared luminescence up to 1070 nm, *Angew. Chem., Int. Ed.*, 2022, **134**, e202208881.
2 C. H. Hu, X. T. Cai, M. F. Wu, Z. H. Yang, J. Han and S. L. Pan, Lone pair-driven enhancement of birefringence in polar alkali metal antimony phosphates, *Chem. Mater.*, 2022, **34**, 4224–4231.
3 W. L. Yin, M. L. Zhou, A. K. Iyer, J. Y. Yao and A. Mar, Noncentrosymmetric quaternary selenide $Ba_{23}Ga_8Sb_2Se_{38}$: Synthesis, structure, and optical properties, *J. Alloys Compd.*, 2017, **729**, 150–155.
4 W. S. Sheldrick and M. Wachhold, chalcogenidometalates of the heavier group 14 and 15 elements, *Coord. Chem. Rev.*, 1998, **176**, 211–322.
5 Y. L. Deng, L. Huang, X. H. Dong, L. Wang, K. M. Ok, H. M. Zeng, Z. E. Lin and G. H. Zou, $K_2Sb(P_2O_7)F$: Cairo pentagonal layer with bifunctional genes reveal optical performance, *Angew. Chem., Int. Ed.*, 2020, **59**, 21151–21156.
6 A. Pfitzner and S. Reiser, Refinement of the crystal structures of Cu_3PS_4 and Cu_3SbS_4 and a comment on normal tetrahedral structures, *Z. Kristallogr. – Cryst. Mater.*, 2002, **217**, 51–54.
7 H. A. Graf and H. Schäfer, Preparation and Crystal Structure of $K_2Sb_4S_7$, *Z. Naturforsch. B*, 1972, **27**, 735–739.
8 E. M. Heppke, S. Klenner, O. Janka, R. Pöttgen, T. Bredow and M. Lerch, Cu_2ZnSbS_4: A thioantimonate(v) with remarkably strong covalent Sb-S bonding, *Inorg. Chem.*, 2021, **60**, 2730–2739.
9 F. Y. Yuan, Y. Z. Huang, H. Zhang, C. S. Lin, G. L. Chai and W. D. Cheng, $Ba_4GeSb_2Se_{11}$: An infrared nonlinear optical crystal with a v-shaped Se_3^{2-} group possessing a large contribution to the SHG response, *Inorg. Chem.*, 2021, **60**, 15593–15598.
10 R. H. Duan, J. N. Shen, C. S. Lin, P. F. Liu, H. Lin, H. Fu, S. Xiong, H. J. Zhao, M. A. Khan and L. Chen, Syntheses, structures, and properties of sulfides constructed by SbS_4 teeter-totter polyhedra: $Ba_3La_4Ga_2Sb_2S_{15}$ and $BaLa_3GaSb_2S_{10}$, *Inorg. Chem. Front.*, 2017, **4**, 123–130.
11 M. C. Chen, L. M. Wu, H. Lin, L. J. Zhou and L. Chen, Disconnection enhances the second harmonic generation response: synthesis and characterization of $Ba_{23}Ga_8Sb_2S_{38}$, *J. Am. Chem. Soc.*, 2012, **134**, 6058–6060.
12 A. Yalikun, K. W. Zhang, J. Han and Z. H. Yang, $LiSrSbS_3$: parallel configurations of lone pair electrons inducing a large birefringence, *Dalton Trans.*, 2022, **51**, 14545–14550.
13 K. Y. Wang, M. L. Feng, X. Y. Huang and J. Li, Organically directed heterometallic chalcogenidometalates containing group 12(II)/13(III)/14(IV) metal ions and antimony(III), *Coord. Chem. Rev.*, 2016, **322**, 41–68.

14 Y. H. Li, X. D. Song, Y. P. Zhong, Y. K. Guo, M. Ji, Z. L. You and Y. L. An, Temperature controlling valance changes of crystalline thioarsenates and thioantimonates, *J. Alloys Compd.*, 2021, **872**, 159591.

15 D. X. Jia, Y. Zhang, Q. X. Zhao and J. Deng, Mixed-valent selenidoantimonates(III,V) with transition-metal complexes as counterions: Solvothermal syntheses and characterization of $[M(dien)_2]_2Sb_4Se_9$ (M=Mn,Fe),$[Co(dien)_2]_2Sb_2Se_6$, and $[Ni(dien)_2]_2Sb_2Se_5$, *Inorg. Chem.*, 2006, **45**, 9812–9817.

16 C. Hu, B. B. Zhang, B. H. Lei, S. L. Pan and Z. H. Yang, Advantageous units in antimony sulfides: exploration and design of infrared nonlinear optical materials, *ACS Appl. Mater. Interfaces*, 2018, **10**, 26413–26421.

17 Y. Lee, J. Jeong, H. J. Lee, M. Kim, D. Han, H. Kim, J. M. Yuk, K. W. Nam, K. Y. Chung and H. G. Jung, Lithium argyrodite sulfide electrolytes with high ionic conductivity and air stability for all-solid-state Li-ion batteries, *ACS Energy. Lett.*, 2021, **7**, 171–179.

18 W. D. Jung, J. S. Kim, Y. J. Kim, H. Jeong, D. Han, K. W. Nam, D. Ahn, D. H. Kwon, H. G. Jung and J. H. Lee, Annealing-free thioantimonate argyrodites with high Li-Ion conductivity and low elastic modulus, *Adv. Funct. Mater.*, 2023, **33**, 2211185.

19 M. J. Li, P. Cheng, G. Q. Luo, J. M. Schoenung and Q. Shen, Effects of Sb oxidation state on the densification and electrical properties of antimony-doped tin oxide ceramics, *J. Mater. Sci.: Mater. Electron.*, 2015, **26**, 4015–4020.

20 P. T. Wood, G. L. Schimek and J. W. Kolis, Synthesis and characterization of novel one-dimensional phases from supercritical ammonia: $Cs_3Ag_2Sb_3S_8$, α-and β-Cs_2AgSbS_4, and Cs_2AgAsS_4, *Chem. Mater.*, 1996, **8**, 721–726.

21 S. Berri, N. Bouarissa, M. Oumertem and S. Chami, First-principles investigation of structural, electronic, optical and thermodynamic properties of KAg_2SbS_4, *Comput. Condens. Matter*, 2019, **19**, e00365.

22 G. L. Schimek, W. T. Pennington, P. T. Wood and J. W. Kolis, Supercritical ammonia synthesis and characterization of four new alkali metal silver antimony sulfides: MAg_2SbS_4 and M_2AgSbS_4 (M=K, Rb), *J. Solid State Chem.*, 1996, **123**, 277–284.

23 S. Mukhopadhyay, D. J. Singh and T. L. Reinecke, Ultralow thermal conductivity in Cs-Sb-Se compounds: Lattice instability versus lone-pair electrons, *Chem. Mater.*, 2020, **32**, 8906–8913.

24 J. Y. Guo, A. Tudi, S. J. Han, Z. H. Yang and S. L. Pan, α-SnF_2: A UV birefringent material with large birefringence and easy crystal growth, *Angew. Chem., Int. Ed.*, 2021, **60**, 3540–3544.

25 A. Das, U. Das and A. K. Das, Relativistic effects on the chemical bonding properties of the heavier elements and their compounds, *Coord. Chem. Rev.*, 2023, **479**, 215000.

26 C. Cui, D. Z. Lu, F. Liang, J. Y. Wang, H. H. Yu and H. J. Zhang, Mid-infrared pulsed nanosecond difference frequency generation of oxide LGN crystal up to 5.7 μm, *Opt. Lett.*, 2021, **46**, 785–788.

27 Y. Z. Wang, J. S. Liu, C. Cui, F. Liang, D. Z. Lu, J. Y. Wang, J. G. Ma, H. J. Zhang, G. Q. Xie and H. H. Yu, Recent progress on acentric $La_3Nb_{0.5}Ga_{5.5}O_{14}$ crystals: large-size growth and application to ultrafast mid-infrared laser systems, *Opt. Mater. Express*, 2022, **12**, 863–875.

28 A. L. Spek, Single-crystal structure validation with the program PLATON, *J. Appl. Crystallogr.*, 2003, **36**, 7–13.

29 O. V. Dolomanov, L. J. Bourhis, R. J. Gildea, J. A. K. Howard and H. Puschmann, OLEX2: a complete structure solution, refinement and analysis program, *J. Appl. Crystallogr.*, 2009, **42**, 339–341.

30 G. M. Sheldrick, SHELXT-Integrated space-group and crystal-structure determination, *Acta Crystallogr., Sect. A: Found. Adv.*, 2015, **71**, 3–8.

31 Z. H. Yang, A. Tudi, B. H. Lei and S. L. Pan, Enhanced nonlinear optical functionality in birefringence and refractive index dispersion of the deep-ultraviolet fluorooxoborates, *Sci. China Mater.*, 2020, **63**, 1480–1488.

32 S. J. Clark, M. D. Segall, C. J. Pickard, P. J. Hasnip, M. I. J. Probert, K. Refson and M. C. Payne, First principles methods using CASTEP, *Z. Kristallogr. – Cryst. Mater.*, 2005, **220**, 567–570.

33 D. R. Hamann, M. Schlüter and C. Chiang, Norm-conserving pseudopotentials, *Phys. Rev. Lett.*, 1979, **43**, 1494–1497.

34 J. P. Perdew, K. Burke and M. Ernzerhof, Generalized gradient approximation made simple, *Phys. Rev. Lett.*, 1996, **77**, 3865.

35 A. M. Rappe, K. M. Rabe, E. Kaxiras and J. D. Joannopoulos, Optimized pseudopotentials, *Phys. Rev. B: Condens. Matter Mater. Phys.*, 1990, **41**, 1227.

36 J. S. Lin, A. Qteish, M. C. Payne and V. Heine, Optimized and transferable nonlocal separable ab initio pseudopotentials, *Phys. Rev. B: Condens. Matter Mater. Phys.*, 1993, **47**, 4174–4180.

37 Y. Wang, B. B. Zhang, Z. H. Yang and S. L. Pan, Cation-tuned synthesis of fluorooxoborates: Towards optimal deep-ultraviolet nonlinear optical materials, *Angew. Chem., Int. Ed.*, 2018, **57**, 2150–2154.

38 B. B. Zhang, G. Q. Shi, Z. H. Yang, F. F. Zhang and S. L. Pan, Fluorooxoborates: Beryllium-free deep-ultraviolet nonlinear optical materials without layered growth, *Angew. Chem., Int. Ed.*, 2017, **56**, 3916–3919.

39 L. Gao, J. B. Huang, S. R. Guo, Z. H. Yang and S. L. Pan, Structure-property survey and computer-assisted screening of mid-infrared nonlinear optical chalcohalides, *Coord. Chem. Rev.*, 2020, **421**, 213379.

40 J. Z. Zhou, Z. X. Fan, K. W. Zhang, Z. H. Yang, S. L. Pan and J. J. Li, $Rb_2CdSi4S_{10}$: novel $[Si_4S_{10}]$ T2-supertetrahedra-contained infrared nonlinear optical material with large band gap, *Mater. Horiz.*, 2023, **10**, 619–624.

41 Y. P. Wang, J. K. Lu, X. Y. Ma, Y. J. Niu, V. Singh, P. T. Ma, C. Zhang, J. Y. Niu and J. P. Wang, Synthesis, characterization and catalytic oxidation of organosilanes with a novel multilayer polyoxomolybdate containing mixed-valence antimony, *Mol. Catal.*, 2018, **452**, 167–174.

42 G. Q. Shi, Y. Wang, F. F. Zhang, B. B. Zhang, Z. H. Yang, X. L. Hou, S. L. Pan and K. R. Poeppelmeier, Finding the Next Deep-Ultraviolet Nonlinear Optical Material: $NH_4B_4O_6F$, *J. Am. Chem. Soc.*, 2017, **139**, 10645.

43 X. F. Wang, Y. Wang, B. B. Zhang, F. F. Zhang, Z. H. Yang and S. L. Pan, CsB_4O_6F: A congruent-melting deep-ultraviolet nonlinear optical material by combining superior functional units, *Angew. Chem., Int. Ed.*, 2017, **56**, 14119–14123.

44 M. Mutailipu, J. Han, Z. Li, F. M. Li, J. J. Li, F. F. Zhang, X. F. Long, Z. H. Yang and S. L. Pan, Achieving the full-wavelength phase-matching for efficient nonlinear optical frequency conversion in $C(NH_2)_3BF_4$, *Nat. Photonics*, 2023, **17**, 694–701.

45 J. Sejkora, E. Buixaderas, P. Škácha and J. Plášil, Micro-Raman spectroscopy of natural members along $CuSbS_2$-$CuSbSe_2$ join, *J. Raman Spectrosc.*, 2018, **49**, 1364–1372.

46 B. W. Liu, X. M. Jiang, S. M. Pei, W. F. Chen, L. Q. Yang and G. C. Guo, Balanced infrared nonlinear optical performance achieved by modulating the covalency and ionicity distributions in the electron localization function map, *Mater. Horiz.*, 2021, **8**, 3394–3398.

47 M. Mutailipu, M. Zhang, B. B. Zhang, L. Y. Wang, Z. H. Yang, X. Zhou and S. L. Pan, $SrB_5O_7F_3$: The first asymmetric alkaline-earth fluorooxoborate with unprecedented $[B_5O_9F_3]^{6-}$ functionalized chromophore, *Angew. Chem., Int. Ed.*, 2018, **57**, 6095–6099.

48 M. Mutailipu, M. Zhang, H. P. Wu, Z. H. Yang, Y. H. Shen, J. L. Sun and S. L. Pan, $Ba_3Mg_3(BO_3)_3F_3$ polymorphs with reversible phase transition and high performances as ultraviolet nonlinear optical materials, *Nat. Commun.*, 2018, **9**, 3089.

49 H. T. Qiu, F. M. Li, Z. Li, Z. H. Yang, S. L. Pan and M. Mutailipu, Breaking the inherent interarrangement of $[B_3O_6]$ clusters for nonlinear optics with orbital hybridization enhancement, *J. Am. Chem. Soc.*, 2023, **145**, 24401–24407.

50 L. A. Wang, C. C. Tu, J. Z. Zhou, Y. Chu, Z. H. Yang, S. L. Pan and J. J. Li, Mixed anionic tetrahedra guided design of new infrared nonlinear optical material $Cs_3Ga_8S_{13}Cl$ with high laser-induced damage threshold, *Adv. Opt. Mater.*, 2024, **12**, 2301634.

51 S. Baroni, S. De Gironcoli, A. Dal Corso and P. Giannozzi, Phonons and related crystal properties from density-functional perturbation theory, *Rev. Mod. Phys.*, 2001, **73**, 515.

52 B. H. Lei, S. L. Pan, Z. H. Yang, C. Cao and D. J. Singh, Second harmonic generation susceptibilities from symmetry adapted Wannier functions, *Phys. Rev. Lett.*, 2020, **125**, 187402.

53 M. Mutailipu, F. M. Li, C. C. Jin, Z. H. Yang, K. R. Poeppelmeier and S. L. Pan, Strong nonlinearity induced by coaxial alignment of polar chain and dense $[BO_3]$ units in $CaZn_2(BO_3)_2$, *Angew. Chem., Int. Ed.*, 2022, **61**, e202202096.

54 Y. Z. Wang, F. Liang, J. Y. Wang, D. Z. Lu, H. H. Yu and H. J. Zhang, Growth of a large-aperture mid-infrared nonlinear optical $La_3Nb_{0.5}Ga_{5.5}O_{14}$ crystal for optical parametric chirped-pulse amplification, *CrystEngComm*, 2021, **23**, 7212–7218.

55 Y. Z. Wang, F. Liang, D. Z. Lu, S. X. Wang, J. Y. Wang, H. H. Yu and H. J. Zhang, Laser damage mechanism and threshold improvement of nonlinear optical $La_3Ga_{5.5}Nb_{0.5}O_{14}$ crystal for a mid-infrared high-intensity laser, *Opt. Mater. Express*, 2022, **12**, 3449–3462.

56 H. W. Jia, D. Xu, Z. J. Li, M. Arif, Y. S. Jiang and X. L. Hou, $(C_3N_6H_7)BF_4 \cdot H_2O$ and $(C_3N_6H_7)SO_3CH_3 \cdot H_2O$ with large birefringence induced by coplanar π-conjugated $[C_3N_6H_7]^+$ groups, *Inorg. Chem. Front.*, 2024, DOI: **10.1039/d4qi01061b**.